Available online at www.sciencedirect.com

ScienceDirect

Procedia Structural Integrity 2 (2016) 358–365

Structural Integrity Procedia

www.elsevier.com/locate/procedia

21st European Conference on Fracture, ECF21, 20-24 June 2016, Catania, Italy

Effect of non-metallic inclusions and shrinkage cavities on the dynamic fracture toughness of a high-strength G42CrMo4 cast steel

S. Henschel[a,*], S. Dudczig[b], L. Krüger[a], C. G. Aneziris[b]

[a] *Institute of Materials Engineering, TU Bergakademie Freiberg, Gustav-Zeuner-Str. 5, 09599 Freiberg, Germany*
[b] *Institute of Ceramic, Glass and Construction Materials, TU Bergakademie Freiberg, Agricolastr. 17, 09599 Freiberg, Germany*

Abstract

The formation and clustering of non-metallic inclusions was investigated by applying a steel casting simulator. In a fully controlled atmosphere, the oxygen content of the steel melt was intentionally increased. At a specified level, the steel was deoxidized by pure aluminum. After the treatment, the melt was cooled down in the crucible. The effects of the inclusions and the cavities were determined by means of metallography, tensile tests, dynamic fracture toughness tests, and fractography. Metallographic results show that alumina particles have a strong tendency to aggregate at the walls of the crucible. Neglecting this aggregation, a relatively homogeneous distribution of alumina inclusions was observed. Furthermore, the solidified steel exhibited manganese sulphide inclusions and shrinkage cavities. The results of the tensile tests revealed a relatively low ductility. Fractographic examinations showed that both non-metallic inclusions and shrinkage cavities promoted ductile fracture. Results of dynamic fracture toughness tests revealed a relatively large scatter in the dynamic crack resistance. This was analogously attributed to the damaging effect of the non-metallic inclusions and the shrinkage cavities. Fractographic investigations showed that not only alumina inclusions but preferentially manganese sulphide inclusions affected the failure behavior of the investigated steel.

Keywords: Non-metallic inclusions; shrinkage cavities; steel casting simulator; dynamic fracture toughness; high-strength steel

1. Introduction

Non-metallic inclusions in a cast steel can originate from the refractory materials or the melt treatment (Zhang and Thomas (2003)). As a result of the deoxidation treatment, oxide inclusion are formed and transferred to the slag. However, a certain amount of oxygen and deoxidation agent (Al) will remain dissolved in the metal melt. During the cooling in the casting process, these elements will form endogenous inclusions (Dekkers et al. (2002)).

It is known that non-metallic inclusions have a detrimental effect on the mechanical properties of metals, such as elongation at fracture (Henschel et al. (2013)). The detrimental effect is the result of the promotion of ductile fracture (Henschel and Krüger (2016)). Ductile fracture initiates preferentially at non-metallic inclusions due to their large size compared to other initiation sites, e.g. carbides (Garrison and Moody (1987)).

* Corresponding author. Tel.: +49-3731-393452 ; fax: +49-3731-393703.
E-mail address: sebastian.henschel@iwt.tu-freiberg.de

10.1016/j.prostr.2016.06.046

The aim of the present study was the formation of endogenous non-metallic inclusions in a 42CrMo4 melt under well-defined conditions, such as temperature and atmosphere. The spatial distribution of these non-metallic inclusions was investigated by means of metallography. Furthermore, the effect on the mechanical properties, especially strength, deformability and fracture toughness, was analyzed.

2. Materials and Methods

The chemical composition of the investigated 42CrMo4 steel is shown in Tab. 1. The processes of melting the steel, increasing the oxygen content, deoxidizing, and, finally, solidification were performed in a steel casting simulator. The Ar atmosphere within this device was fully controlled. The steel was melted by an induction heating system which was also used to stir the melt within the crucible made of Al_2O_3/Al-Mg-spinel. Details of the steel casting simulator can be found in Aneziris et al. (2013). The oxygen level was increased by the addition of Fe_2O_3. The deoxidizing treatment was done by pure Al. The evolution of the temperature and the oxygen content during the melt treatment is shown in Fig. 1a. After this treatment, the heating was turned off, and the melt cooled freely in the crucible. The solidified steel had a cylindrical shape (radius $R = 110$ mm, height $H = 135$ mm).

In order to investigate the spatial distribution of the formed alumina inclusions, samples were cut from different locations from the cylinder, see Fig. 1b.

The samples were ground and polished up to 1 µm diamond grain size. The area of interest of each sample (approx. 100 mm^2) was scanned by an optical microscope (Olympus XC-10) and analyzed by an automated image analysis software (Particle Inspector). This software determined the position and the size of alumina inclusion. In a second step, the distribution of MnS inclusions was measured at selected positions. The size of the inclusion was defined in terms of the equivalent circle diameter (ECD).

Samples for mechanical characterization were heat treated. This treatment consisted of austenitizing (840 °C, 20 min, vacuum), quenching in a stream of He (equal to quenching in oil), and tempering (560 °C, 1 h, N_2).

Quasi-static tensile tests ($\dot{\varepsilon} \approx 5 \cdot 10^{-4}\,s^{-1}$) were performed in an electro-mechanical universal testing machine (Zwick 1476) applying the specimen geometry B5×25 according to DIN (2009). A servo-hydraulic universal testing machine (MTS 810) and an instrumented drop tower were utilized for tensile tests at intermediate strain rates of approximately $1\,s^{-1}$ and dynamic tensile tests ($\dot{\varepsilon} \approx 10^{2}\,s^{-1}$), respectively. At the two last-mentioned tests, a special specimen geometry was applied to measure the force close to the gauge length. A purely elastically deforming part of

Table 1. Chemical composition of investigated steel.

C	Cr	Mo	Mn	Si	Al	S	P	Fe
0.41	1.03	0.19	0.77	0.25	0.021	0.031	0.012	balance

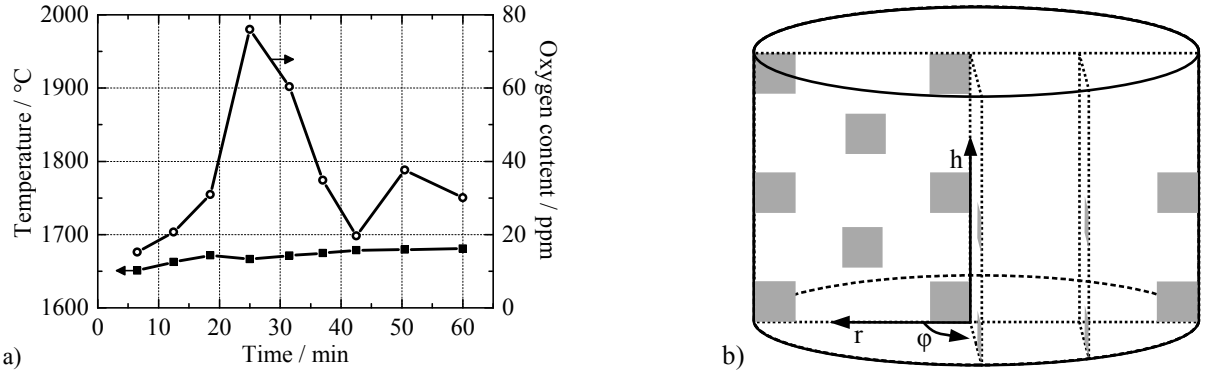

Fig. 1. (a) Evolution of temperature and oxygen content during melt treatment; (b) Positions of samples for metallographic investigations. The positions were defined with cylindrical coordinates (radius r, angle φ, height h).

the specimen was equipped with strain gauges which were calibrated. Details can be found in Nemat-Nasser (2000). The gauge length of those specimens was shorter ($l_0/d_0 = 3$). Hence, the elongation at fracture was converted to A_5 which refers to $l_0/d_0 = 5$:

$$A_5 = \left(1 - \frac{3}{5}\right) \cdot A_\mathrm{u} + \frac{3}{5} \cdot A_3 \tag{1}$$

This equation was adopted from Reinders (1992) and assumes that the uniform elongation (A_u in percent) and the elongation during necking (in mm) are independent of the l_0/d_0 ratio. The reduction of area is denoted as Z.

Dynamic fracture toughness tests were performed in an instrumented Charpy impact testing machine at room temperature. The specimen size of 55×10×10 mm^3 (length L, width W, thickness B) was applied. The specimens were fatigue precracked up to an initial crack length a_0 of $a_0/W \approx 0.5$ and then side-grooved (net thickness $B_\mathrm{N} = 8$ mm). Impact energies of 15 J were chosen in order to obtain a reasonable combination of high loading rates ($\dot{K} \approx 2.6 \cdot 10^5$ MPa m$^{0.5}$ s^{-1}) and relatively small oscillations of the force signal.

The loading of the specimen was not only measured by the instrumented tup, but also by a strain gauge (SG) near the crack tip. This strain gauge was calibrated statically in a servo-hydraulic universal testing machine up to a force of approx. 1.1 kN (11.5 MPa m$^{0.5}$) in order to maintain a small plastic zone.

The load point displacement was calculated by the double integration of the force-time signal (Henschel and Krüger (2015)). In contrast to the tests of Henschel and Krüger (2015) (low-blow tests), the laser-based deflection measurement was not evaluated. During the present impact tests the relatively high oscillations of the reflective tape were measured.

The samples exhibited unstable fracture after a certain amount of non-linear behavior. This non-linear behavior was attributed to stable crack extension which was larger than 0.2 mm. The toughness at the point of instability was calculated in terms of a critical J integral (ISO (2002)):

$$J_\mathrm{u} = J_\mathrm{e} + J_\mathrm{p} = \frac{(1-\nu^2)K^2}{E} + \frac{2U_\mathrm{p}}{B_\mathrm{N}(W-a_0)} \tag{2}$$

with the elastic and plastic part of the J integral J_e and J_p, respectively, the stress intensity factor K, and the plastic work U_p.

The strain rate $\dot{\varepsilon}$ during the dynamic fracture mechanics tests was estimated by Irwin (1964):

$$\dot{\varepsilon} = \frac{2 \cdot R_{\mathrm{p}0.2}(\dot{\varepsilon})}{t \cdot E} \tag{3}$$

In Eq. (3), $R_{\mathrm{p}0.2}(\dot{\varepsilon})$ is the 0.2 % offset yield strength at the strain rate $\dot{\varepsilon}$, t is the time up to the point of instability, and E is the Young's modulus.

The fracture surfaces were investigated by means of scanning electron microscopy (SEM). Information on the chemical composition of the non-metallic inclusions was obtained by energy dispersive X-ray diffraction (EDX).

3. Results and Discussion

3.1. Metallographic observations

Fig. 2 shows the position of alumina and manganese sulphide inclusions and their respective sizes (scaled). It was observed that a large amount of alumina inclusions was aggregated near the crucible (Fig. 2a and c). Hence, aggregating the non-metallic inclusions at the crucible wall is a possibility to remove the alumina inclusions from the

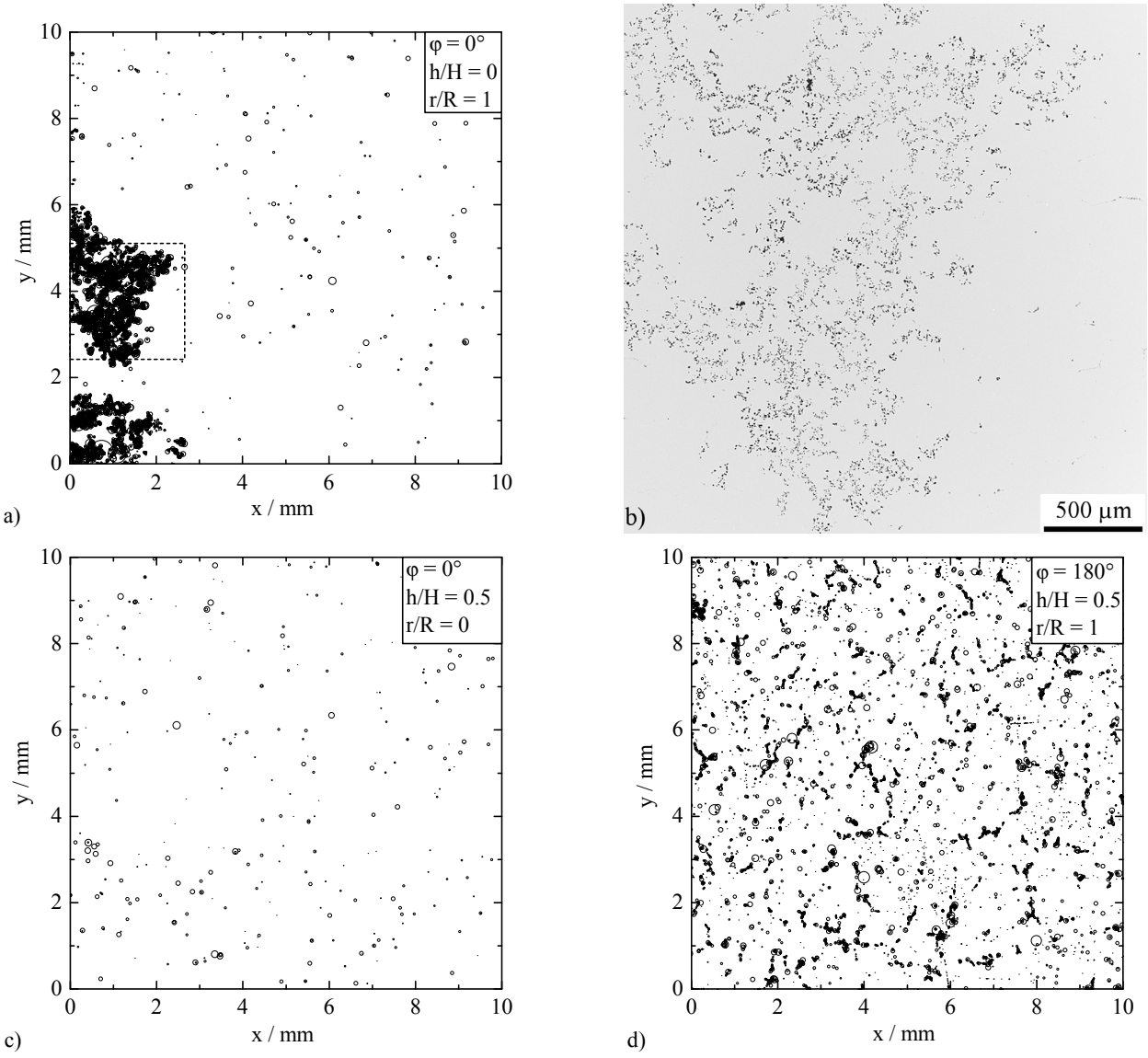

Fig. 2. (a) Aggregation of alumina inclusions near the crucible (left); (b) Optical micrograph from subfigure a; (c) Low amount of aggregation in the center of the cylinder; (d) Distribution of manganese sulphides. The diameters of the circles in a, c and d are equal to the 10-fold equivalent circle diameter (ECD).

melt. In Fig. 2c, the area of the micrograph shown in subfigure d is marked. In contrast, inner regions of the cylinder (Fig. 2b) exhibited only small amounts of aggregated alumina inclusions. Such an aggregation is typical for alumina inclusions (Zhang (2013)). Since the regions near the crucible wall could not be used for mechanical testing, only the inner regions were analyzed in terms of particle size and distance distribution.

Fig. 3 shows the distribution of size and distance of alumina inclusions as a function of the position within the cylinder. It can be seen that the median size of the alumina inclusions was below 5 µm. These small inclusions clustered as was shown in Fig. 2.

It was observed that MnS inclusions initiated the ductile fracture in most cases (see below). Fig. 4 shows the size distribution of MnS inclusions. From Figs. 3 and 4 it becomes apparent that the MnS inclusions, as measured by means of metallography, were in the same size range as the alumina inclusions. However, the distances between these MnS

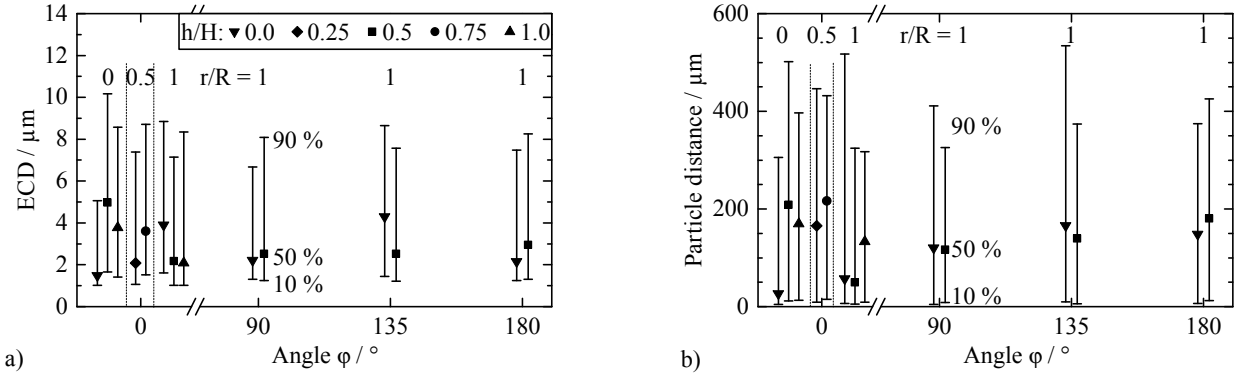

Fig. 3. Distribution of alumina inclusions (inclusions near the crucible were neglected). (a) Distribution of ECD; (b) Distribution of distances.

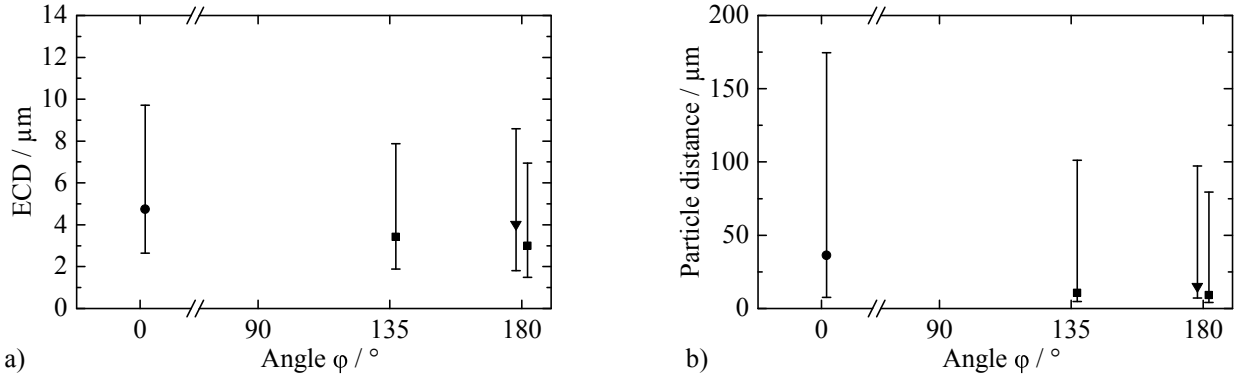

Fig. 4. Distribution of MnS inclusions (inclusions near the crucible were neglected). (a) Distribution of ECD; (b) Distribution of distances. The definition of symbols is the same as in Fig. 3.

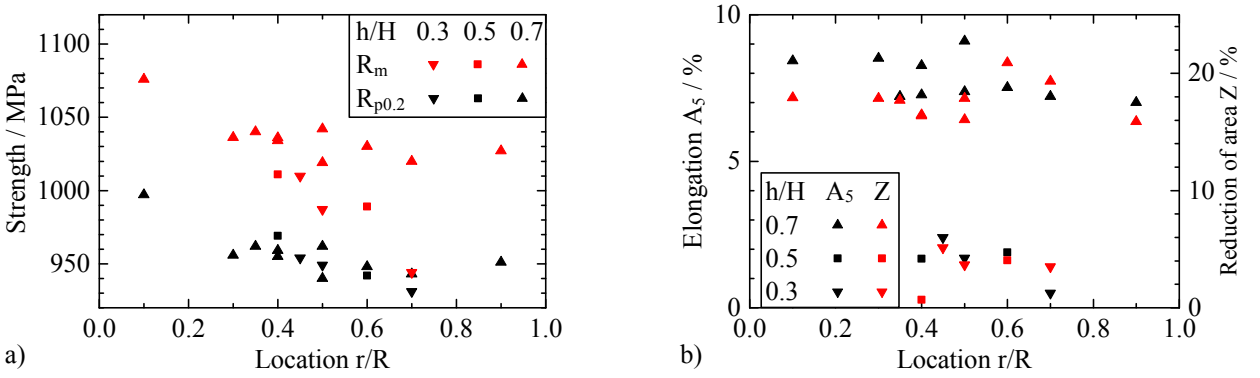

Fig. 5. Dependence of $R_{p0.2}$ and R_m (a), and A_5 and Z (b) on the position within the cylinder. Solid/open symbols: sample direction vertical/horizontal. $T = 20\,°C$.

inclusions were significantly smaller. The measurement of small distances between the MnS inclusions was attributed to Type II MnS (dendritic shape) which were cut at an arbitrary plane.

3.2. Mechanical properties

The effect of the position on the strength and ductility is presented in Fig. 5. In Fig. 5a, it can be seen that $R_{p0.2}$

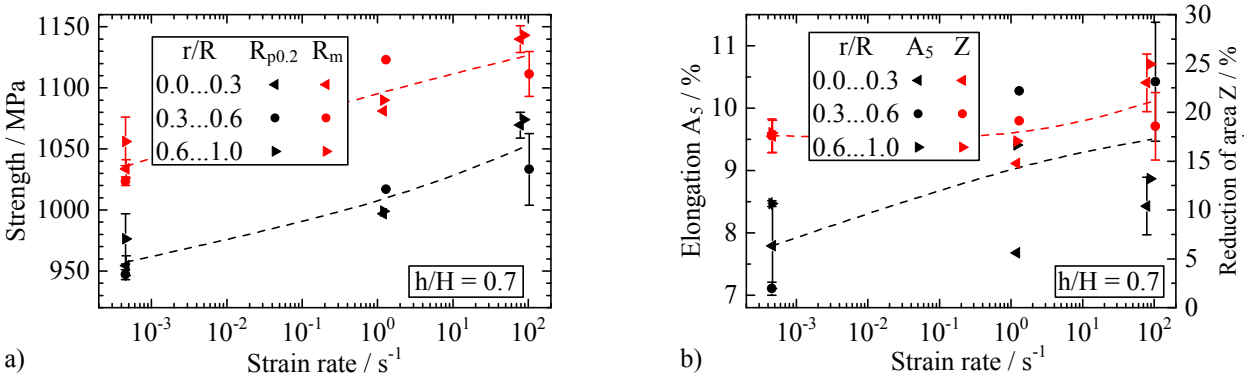

Fig. 6. (a) Increase of $R_{p0.2}$ and R_m with strain rate $\dot{\varepsilon}$; (b) No effect of $\dot{\varepsilon}$ on A_5 and Z. There is no effect of the radial position. Dashed lines represent mean values at each strain rate.

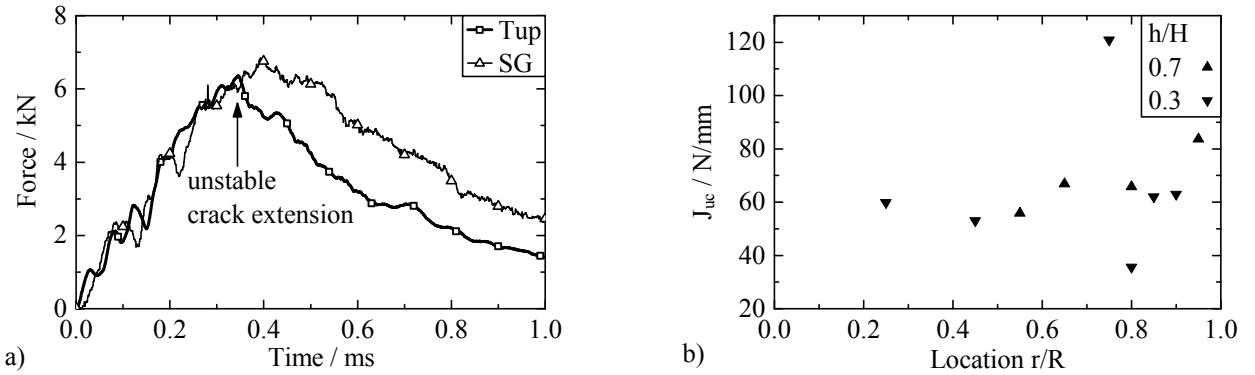

Fig. 7. (a) Typical force-time-plot. The force was measured by the instrumented tup and a calibrated strain gauge (SG) near the crack tip. $\dot{\varepsilon} \approx 20\,\mathrm{s}^{-1}$ (Eq. (3)); (b) J integral at the point of instability. $J_{max} \approx 250\,\mathrm{N/mm}$ (ISO (2002)).

and R_m depended only slightly on the radial position (r/R) within the cylinder. Furthermore, there was no effect of the axial position (h/H) on $R_{p0.2}$. It becomes apparent from Fig. 5b that r/R had no effect on the ductility when the sample was taken from the top of the cylinder. However, a sample position near the bottom of the cylinder resulted in a relatively low ductility (A_5 and Z). Furthermore, such a position also decreased R_m. Hence, the ability for strain hardening was reduced.

The effect of the strain rate on the strength and ductility behavior is shown in Fig. 6. As can be seen in Fig. 6a, the strength ($R_{p0.2}$ and R_m) increased with increasing strain rate. In Fig. 6b, a relationship between the ductility, A_5 and Z, and the strain rate was not determinable due to the scatter of the tests. A possible increase in A_5 and Z at the highest strain rate was attributed to deformation heat which resulted in a increase in temperature during the test.

Results of the dynamic fracture toughness tests are presented in Fig. 7. In Fig. 7a, it can be seen that shortly after impact of the tup, there is a difference of the force determined by the two methods. This difference was attributed to inertia of the specimen and is a known issue (Saxton et al. (1974); Böhme and Kalthoff (1982)). At the point of unstable crack extension, there was no difference between the forces measured by the tup and the specimen's strain gauge. Hence, the force measured by the tup can be used to evaluate the specimen loading. Furthermore, quasi-static assumptions, i. e. neglecting inertia of the specimen, can be applied to calculate the J integral (Eq. (2)).

Prior to instability, a certain amount of non-linear behavior was measured (Fig. 7a). As is shown below, the amount of stable fracture was larger than 0.2 mm. The corresponding toughness J_u is given in Fig. 7b. As was observed for the deformability, the toughness was also independent of the radial position. Furthermore, there was no effect of the axial position on the toughness.

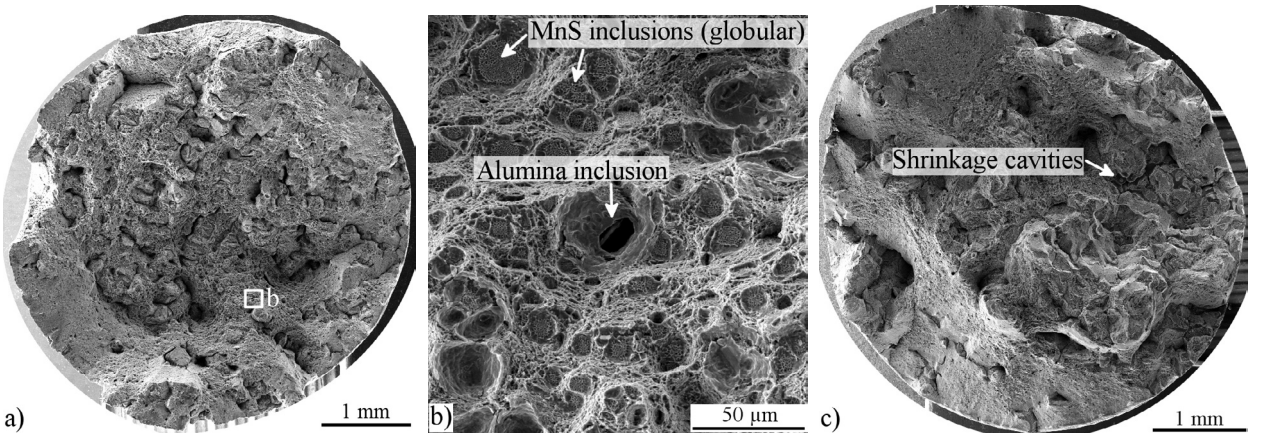

Fig. 8. Typical fracture surfaces of samples with relatively high (a) and low (c) ductility. (b) Detail form subfigure a: Alumina inclusion. $\dot{\varepsilon} = 4 \cdot 10^{-4}\,\mathrm{s}^{-1}$.

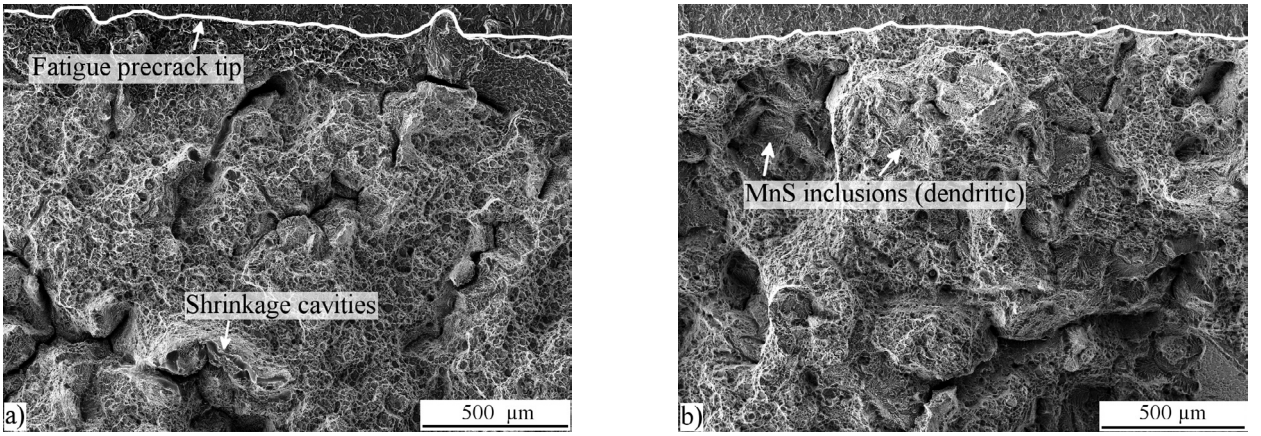

Fig. 9. Fracture surfaces of samples with relatively low (a) and high (b) toughness. (a) $r/R = 0.8$; (b) $r/R = 0.75$.

3.3. Fracture surfaces

Reasons for the relatively low ductility shown in Fig. 5 can be observed on the fracture surfaces, Fig. 8. Obviously, shrinkage cavities caused the relatively low ductility of the sample in Fig. 8c ($A_5 = 1.7\,\%, Z = 0.7\,\%$). Shrinkage cavities in the solidified steel were attributed to insufficient feeding in the lower part of the cylinder. In contrast, the sample in Fig. 8a revealed $A_5 = 7.5\,\%$ and $Z = 20.9\,\%$. Not only MnS inclusions and shrinkage cavities, but also alumina inclusions were found (verified by EDX). In Fig. 8b, large void growth associated with such an alumina inclusion was observed.

Fracture surfaces of the dynamic fracture toughness tests are shown in Fig. 9. In Fig. 9a, a relatively large amount of shrinkage cavities was found. Furthermore, MnS inclusions, as shown in Fig. 9b, were present at each fracture surface. These MnS inclusions had a dendritic morphology (Type II) and cover large areas. Additionally, small globular MnS inclusions (Type I) were observed, see Fig. 8b. Banks and Gladman (1979) analogously found the detrimental effect of type II sulphides compared to type I sulphides.

4. Conclusions and Outlook

A steel casting simulator was applied to generate endogenous alumina inclusions. Additional to these intentionally formed non-metallic inclusions, MnS inclusions were also formed due to the relatively high sulfur content of the steel.

The steel was then characterized with respect to the distribution of non-metallic inclusions, the mechanical properties and the resulting fracture surfaces. The observations of the present study can be summarized as follows:

The intentionally formed Al_2O_3 inclusions were mainly found near the crucible within a distance of approximately 2–3 mm. Within this part of the cylinder, cutting of samples for mechanical testing was not possible.

There was only a slight dependency of the strength on the radial and axial position within the cylinder. In contrast, only samples from the top of the cylinder ($h/H = 0.7$) exhibited the highest deformability (A_5 and Z).

An increase in strain rate resulted in an increase of strength. However, no effect of the strain rate on the deformability was detected.

The dynamic fracture toughness tests revealed unstable crack propagation after a small amount stable tearing. The MnS inclusions and the shrinkage porosity were the main failure initiators. Due to the dendritic shape of the MnS inclusions, the crack was initiated after small plastic deformation. Nevertheless, the crack initiation and growth was achieved by ductile fracture. Only small amounts of cleavage fracture were observed. The Al_2O_3, which was intentionally formed during the melt treatment, was found on the fracture surface in relatively small amounts.

In further studies, the aggregation of alumina inclusions at the crucible wall should be investigated more in detail. Different types of crucible material or coating of the crucible should be tested.

Acknowledgements

The authors thank the German Research Foundation (DFG) for the financial support of the investigations in the Collaborative Research Center 920, subproject C05. The support of Birgit Witschel with the metallographic inspection is greatly appreciated.

References

Aneziris, C.G., Dudczig, S., Hubálková, J., Emmel, M., Schmidt, G., 2013. Alumina coatings on carbon bonded alumina nozzles for active filtration of steel melts. Ceram. Int. 39, 2835–2843. doi:10.1016/j.ceramint.2012.09.055.

Banks, T.M., Gladman, T., 1979. Sulphide shape control. Met. Technol. 6, 81–94. doi:10.1179/030716979803276273.

Böhme, W., Kalthoff, J.F., 1982. The behavior of notched bend specimens in impact testing. Int. J. Fract. 20, R139–R143. doi:10.1007/BF01130620.

Dekkers, R., Blanpain, B., Wollants, P., Haers, F., Vercruyssen, C., Gommers, B., 2002. Non-metallic inclusions in aluminium killed steels. Ironmak. Steelmak. 29, 437–444. doi:10.1179/030192302225004584.

DIN, 2009. DIN 50125. Prüfung metallischer Werkstoffe – Zugproben.

Garrison, Jr., W.M., Moody, N.R., 1987. Ductile fracture. J. Phys. Chem. Solids 48, 1035–1074. doi:10.1016/0022-3697(87)90118-1.

Henschel, S., Krewerth, D., Ballani, F., Weidner, A., Krüger, L., Biermann, H., Emmel, M., Aneziris, C.G., 2013. Effect of filter coating on the quasi-static and cyclic mechanical properties of a G42CrMo4 casting. Adv. Eng. Mater. 15, 1216–1223. doi:10.1002/adem.201300125.

Henschel, S., Krüger, L., 2015. Deflection measurement in low-blow Charpy impact tests. MP Mater. Test. 57, 837–842. doi:10.3139/120.110785.

Henschel, S., Krüger, L., 2016. Modelling of crack initiation in a G42CrMo4 steel with non-metallic inclusions. Steel Res. Int. 87, 29–36. doi:10.1002/srin.201400567.

Irwin, G.R., 1964. Crack-toughness testing of strain-rate sensitive materials. J. Eng. Power (Trans. ASME) 86, 444–450. doi:10.1115/1.3677632.

ISO, 2002. ISO 12135. Metallic materials – Unified method of test for the determination of quasistatic fracture toughness.

Nemat-Nasser, S., 2000. High strain rate tension and compression tests, in: Kuhn, H., Medlin, D. (Eds.), ASM-Handbook. ASM International, Ohio. volume 8, pp. 429–446.

Reinders, B.O., 1992. Beitrag der mechanischen Zwillingsbildung zum Festigkeits- und Verformungsverhalten von Armco-Eisen. Ph.d. thesis. Technische Universität Clausthal.

Saxton, H.J., Ireland, D.R., Server, W.L., 1974. Analysis and control of inertial effects during instrumented impact testing, in: DeSisto, T.S. (Ed.), Instrumented impact testing. American Society for Testing and Materials, Philadelphia. volume 563 of *ASTM STP*, pp. 50–73. doi:10.1520/STP32185S.

Zhang, L., 2013. Nucleation, growth, transport, and entrapment of inclusions during steel casting. JOM J. Miner. Met. Mater. Soc. 65, 1138–1144. doi:10.1007/s11837-013-0688-y.

Zhang, L., Thomas, B.G., 2003. State of the art in evaluation and control of steel cleanliness. ISIJ Int. 43, 271–291. doi:10.2355/isijinternational.43.271.